ADVANCED MATERIALS
www.advmat.de

High-Current-Density Organic Electrochemical Diodes Enabled by Asymmetric Active Layer Design

Youngseok Kim, Gunwoo Kim, Bowen Ding, Dahyun Jeong, Inho Lee, Sungjun Park, Bumjoon J. Kim, Iain McCulloch, Martin Heeney, and Myung-Han Yoon**

Owing to their outstanding electrical/electrochemical performance, operational stability, mechanical flexibility, and decent biocompatibility, organic mixed ionic–electronic conductors have shown great potential as implantable electrodes for neural recording/stimulation and as active channels for signal switching/amplifying transistors. Nonetheless, no studies exist on a general design rule for high-performance electrochemical diodes, which are essential for highly functional circuit architectures. In this work, generalizable electrochemical diodes with a very high current density over 30 kA cm^{-2} are designed by introducing an asymmetric active layer based on organic mixed ionic–electronic conductors. The underlying mechanism on polarity-sensitive balanced ionic doping/dedoping is elucidated by numerical device analysis and in operando spectroelectrochemical potential mapping, while the general material requirements for electrochemical diode operation are deduced using various types of conjugated polymers. In parallel, analog signal rectification and digital logic processing circuits are successfully demonstrated to show the broad impact of circuits incorporating organic electrochemical diodes. It is expected that organic electrochemical diodes will play vital roles in realizing multifunctional soft bioelectronic circuitry in combination with organic electrochemical transistors.

1. Introduction

Recently, organic electrochemical transistors (OECTs) have emerged as attractive building blocks in the design of multifunctional bioelectronic devices. Owing to the nature of organic mixed ionic–electronic conductors (OMIECs) as an active channel, OECTs need to be operated in ion-rich environments, such as aqueous[1–3] and/or polymeric gel electrolytes,[4–6] with highly interactive interfacial areas. Accordingly, subtle changes in a given electrochemical environment can be effectively translated into instrument-friendly electrical signals with excellent amplification performance, as characterized by very high transconductance or their geometry-independent benchmark parameter (μC^*; product of carrier mobility and volumetric capacitance) of OECTs.[7–11] OMIECs have been successfully employed for transducing/amplifying electrochemical potentials derived from chemical species,[12–16] electroactive cells and tissues/organs,[17–21] in combination with oscilloscopes and/or data acquisition systems. In parallel, recent advances in various printing/fabrication techniques,[22–24] low-voltage (<1 V) device operation, and high operational stability, have enabled the realization of highly functional analog/digital circuits based on unconventional electronic materials.[22,25–28]

In modern electrical-circuit architectures, resistors, capacitors, transistors, and diodes are all essential for multifunctional operations. Acquired signals can be switched on/off or amplified by transistors, divided by resistors, and stored in capacitors, while diodes play important roles in rectification, device protection, and analog/digital signal processing. Given this

---

Y. Kim, G. Kim, M.-H. Yoon
School of Materials Science and Engineering
Gwangju Institute of Science and Technology
Gwangju 61005, Republic of Korea
E-mail: mhyoon@gist.ac.kr

B. Ding, M. Heeney
Department of Chemistry and Centre for Processable Electronics
Imperial College London
London W12 0BZ, UK
E-mail: m.heeney@imperial.ac.uk

D. Jeong, B. J. Kim
Department of Chemical and Biomolecular Engineering
Korea Advanced Institute of Science and Technology
Daejeon 34141, Republic of Korea

I. Lee, S. Park
Department of Electrical and Computer Engineering
Ajou University
Suwon 16499, Republic of Korea

I. McCulloch
KAUST Solar Center
Division of Physical Sciences and Engineering
King Abdullah University of Science and Technology
Thuwal 23955-6900, Saudi Arabia

I. McCulloch
Department of Chemistry
University of Oxford
Oxford OX1 3TA, UK

The ORCID identification number(s) for the author(s) of this article can be found under https://doi.org/10.1002/adma.202107355.

DOI: 10.1002/adma.202107355

importance, various approaches have been reported towards developing rectifying devices using organic-based materials, such as heterojunction diodes[29–33] (e.g., p–n junction and Schottky barrier diodes), electrochemical diodes,[34,35] polyelectrolyte gel diodes,[36–38] microfluidic/bioinspired ionic diodes,[39–44] and light-emitting electrochemical cell-based current rectifiers.[45–48] These devices rectify electronic/ionic current signals by introducing energy band-bending at the interface of the electronic/ionic heterojunction, driven by an electrical/electrochemical potential gradient between two electrodes. However, the heterojunction configuration typically involves difficulties in implementing conventional diode operation, which requires delicate energy level alignment at the heterogeneous material interface under ion-rich environments. Additionally, most of the previous diode studies do not guarantee fabrication compatibility with other OMIEC-based passive/active components, which are essential to realize multifunctional integrated devices and circuits. One possible solution to the abovementioned issues is the diode-connected transistor configuration using an accumulation-mode OECT device (i.e., electrical connection between gate and drain electrodes), as commonly demonstrated in the complementary metal–oxide–semiconductor (CMOS) manufacturing. In the case of electrochemical devices, however, each gate electrode should be immersed in the designated electrolyte or located nearby the channel with the large-sized electrochemical electrode, such that the diode-connected transistor cannot become a perfect alternative to the desired electrochemical diode for enabling highly integrated multifunctional circuits. Accordingly, a novel device architecture is needed to realize conventional diode functions using OMIECs with a minimal device footprint, which can lead to the fabrication of fully functional integrated circuits responsive to unconventional electrical/electrochemical stimuli originating from physiologically relevant aqueous electrolyte environments. Furthermore, it is highly desired that this novel electrochemical diode design should be generalized to apply various types of OMIEC materials, as long as they meet specific requirements.

Herein, we report on high-performance organic electrochemical diodes (OECDs) and their utilization in functional analog/digital circuits. By defining an asymmetric lateral pattern of organic mixed ionic–electronic conductor on two metallic electrodes, the efficient doping/dedoping of the active layer was enabled under the specific polarity of an applied potential, so that the resultant devices could perform the rectification with an outstanding current density under a low operation voltage of 0.6 V. The basic mechanism on polarity-sensitive balanced ionic doping/dedoping was investigated by numerical device analysis and in operando spectroelectrochemical potential mapping, and the general material requirements for electrochemical diode operation are discussed using various OMIECs (i.e., p- and n-types). Finally, a high-performance OECD architecture with a current density in excess of 30 kA cm^{-2} was fabricated, while OECD-based analog full-wave rectifiers and digital logic processing circuits were implemented.

2. Results and Discussions

To demonstrate the concept of electrochemical diode operation in the presence of aqueous electrolytes, we designed a novel device structure with a specific lateral pattern of OMIECs on the drain and source (**Figure 1**a), to introduce either focused or dispersed ionic doping/dedoping on the active layer, depending on the polarity of the applied potential. The asymmetric geometry of a given active layer was labeled with the degree of asymmetry (DoA), which is defined by the ratio between the active-drain contact area (A_D) and the active-drain/source contact area ($A_D + A_S$) (Figure 1b). Although the operation of the proposed electrochemical diode device can be demonstrated using various types of OMIECs (vide infra), we selected PgBT(F)2gTT (Figure 1c; see Experimental section for details) as the active layer of the representative device owing to its large volumetric capacitance (>150 F cm^{-3}), high carrier mobility (>1 cm^2 V^{-1} s^{-1}), and decent operational stability in air.[49] Since PgBT(F)2gTT is a p-type semiconductor in an accumulation-mode OECT (Figure S1, Supporting Information), the active layer becomes doped under negative gate voltage (V_{GS}, i.e., positive potential on the active layer; E), resulting in an increase not only in carrier mobility (μ) but also in volumetric capacitance (C^*), which indicates the specific capacitance per volume of the active layer, as depicted in the μ–C^* plot (Figure 1d). Considering the OECT operation under negative V_{GS}, the potential of the applied V_{GS} is fully engaged on the active material via ionic-conduction pathway (Figure 1e),[50] resulting in an energy level shift of the active layer toward the valence band (VB). In parallel, the energy level of the active layer in the channel region is bent by the potential difference between the drain and source (V_{DS}), so that the charge carriers in the valence band could drift via electronic-conduction pathway (Figure 1f). It is noteworthy that in an OECT device, the potential values of the drain and source electrodes are fully governed by the gate electrode. However, in the case of an OECD device that lacks the gate electrode, the potential values of drain and source electrodes are not fixed by the gate electrode but floating with the OMIEC oxidation potential (E^0). Simultaneously, there is an ionic-conduction pathway between the drain and source through the electrolyte which is equivalent to two electrochemical capacitors in series (see circuit diagrams in Figure 1g). In the case of the symmetric active layer ($A_D = A_S$; DoA = 50%, Figure 1gi), both capacitors exhibit the same capacitance value, so that there are identical potential drops at both drain–electrolyte and source–electrolyte interfaces (Figure 1hi). Supposing that the capacitance of the active material is uniform regardless of applied potential, the potential distribution profile at a given positive bias between the drain and source should be the mirror image of that at the corresponding negative bias. Accordingly, the energy level shifts from the balanced Fermi level at E^0 ($E°_f$) by the positive and negative V_{DS} are symmetric with respect to the channel region, resulting in the symmetric (bipolar) I–V characteristic (Figure 1ii). In the case of asymmetric active layer ($A_D > A_S$; DoA > 50%, Figure 1gii), the capacitance of the active layer on the drain is larger than that on the source, so that the potential drop at the source–electrolyte interface is significantly larger than that at the drain–electrolyte interface since the same number of ionic charges are stored/released on the active layer on the drain and source (vide infra). Therefore, the potential at the active layer in contact with the small-area source becomes more significantly modulated than that in contact with the large-area drain at the applied V_{DS} (Figure 1hii). So, under positive/negative V_{DS}, the energy level

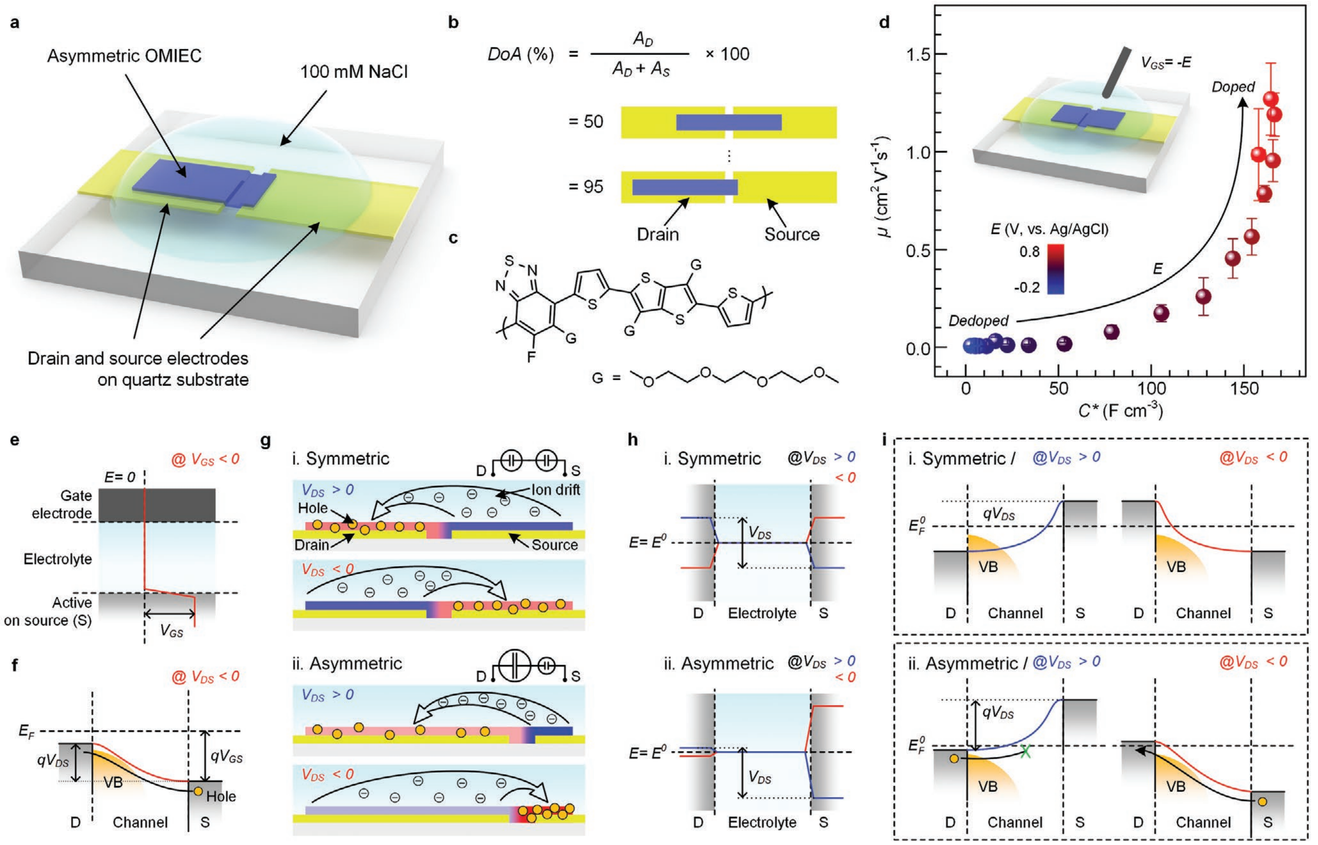

Figure 1. Fundamentals of organic electrochemical diodes. a) A schematic of organic electrochemical diodes based on an asymmetric active layer on the drain and source. b,c) Definition of degree of asymmetry (DoA) (b) and active material structure (PgBT(F)2gTT) (c). d) A plot of μ vs C^* as a function of E (= −0.2 to +0.8 V). Inset shows a conventional OECT device. e,f) Schematic illustrations of the potential diagram in the ionic pathway through the electrolyte (e), and the energy diagram in the electronic pathway through the channel (f) of which potential values were determined by Ag/AgCl gate electrode. g) Ionic behavior of symmetric (i) and asymmetric (ii) OECDs under positive/negative V_{DS}. Each inset depicts an ionic circuit between the drain and source for the symmetric/asymmetric case. h,i) Schematic illustrations of potential (h) and energy (i) in the case of symmetric/asymmetric active layers under positive (blue) and negative V_{DS} (red).

of the active layer in contact with the small-area source substantially increases/decreases to the forbidden (i.e., nonconductive)/valence band (i.e., hole-conductive) region, leading to the asymmetric (unipolar) I–V characteristic (Figure 1iii).

It is noteworthy that while both OECD and OECT consist of two metallic pads and patterned active/passivation layers with an electrochemical cell in contact, the differences between these two device architectures are: i) OECD/OECT require two (i.e., drain and source)/three terminals (i.e., drain, source, and gate), ii) they have electrochemically floated/fixed potential at the active layer and, iii) they have restricted (i.e., asymmetric)/nonrestricted designs of the active layer, respectively.

To demonstrate the polarity dependent focused/dispersed doping/dedoping and the consequent diode behavior in a more systematic way, we extracted electrical/electrochemical properties of the asymmetric channel as a function of DoA. First, the capacity of electrochemical doping/dedoping was determined by measuring the electrochemical capacitance (C) of the active layer. As the PgBT(F)2gTT layer is electrochemically doped under a positive potential on the active layer (E, vs Ag/AgCl reference electrode), its volumetric capacitance increases with the applied potential (**Figure 2**a). In the OECD structure, the total number of ionic charges that the drain and source lose/gain at given potential and DoA are correlated with each other, according to the definition of capacitance ($C = \mathrm{d}Q/\mathrm{d}V$ where Q and V are number of charges and voltage, respectively) and the law of charge conservation (i.e., $Q_D = Q_S$).

$$\int_{E^0}^{(E^0+V_D^0)} C^* \times (DoA)\,\mathrm{d}V = \int_{E^0}^{(E^0+V_D^0)} C^* \times (1 - DoA)\,\mathrm{d}V \tag{1}$$

where V^0_D and V^0_S represent the potentials of the active layer in contact with the drain and source electrodes, respectively, shifted from E^0 when the V_{DS} is applied between the drain and source. The E^0 value of PgBT(F)2gTT was measured as ≈0.3 V (vs Ag/AgCl reference electrode) in aqueous 100 × 10^{-3} M NaCl electrolyte, and those of all OMIECs used for OECD fabrication in this study are depicted in Figure S2 (Supporting Information). Figure 2b depicts the relative number of charges induced in the active material at the drain (left) and source (right), for devices of varying DoA (depicted by color gradient) from 50 (black) to 95% (blue), under an applied negative V_{DS} (each curve was normalized against the number of

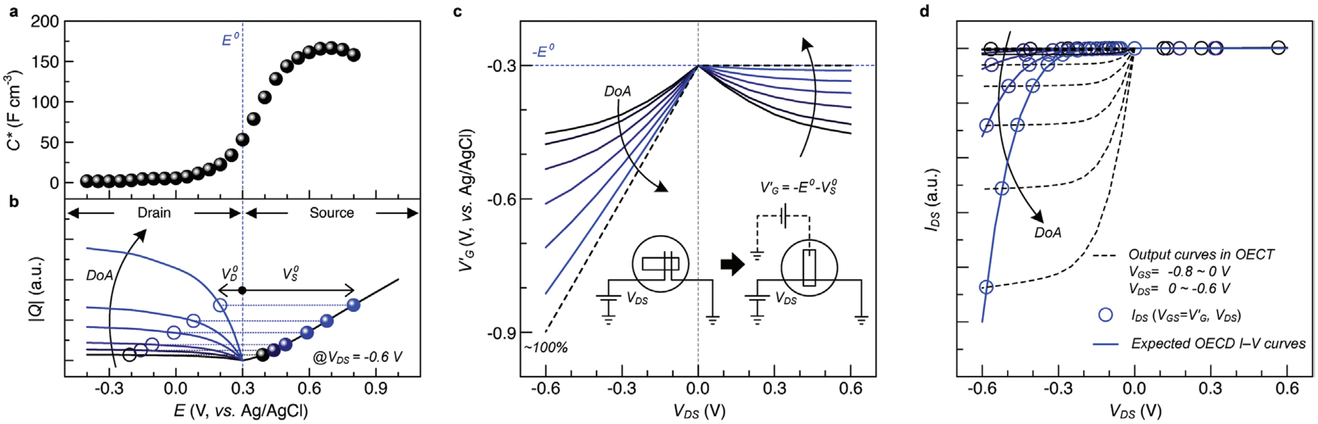

Figure 2. Numerical simulation of OECD devices. a) A plot of C^* as a function of E (= –0.4 to 0.8 V, vs Ag/AgCl), and b) plots of extracted ionic charges (Q; normalized with those on the active layer on source) under negative V_{DS} by varying the DoA from 50 (black) to 95% (blue). The left and right sides with respect to E^0 (= 0.3 V; dashed line, vs Ag/AgCl) depict the number of charges lost from the active layer on the drain and gained by the active layer on the source, respectively. The solid/open symbols indicate the extracted ionic charges at designated E values on the source (V^0_S) and drain (V^0_D) when V_{DS} = –0.6 V is applied. c) Numerically extracted V'_G and d) *I–V* characteristic curves by varying DoA from 50 (black) to 95% (blue) under the V_{DS} from –0.6 to 0.6 V. In (c), the dashed line depicts potential profiles at DoA = 100%, and the inset shows the gate-less OECT model (right) equivalent to the proposed OECD (left). In (d), the dashed lines show normalized output curves of PgBT(F)2gTT-based OECTs under the biases of V_{DS} (= –0.6) and V_{GS} (= –0.8–0 V, with an interval of 0.05 V). Correlated I_{DS} values (open symbol) under the identical bias conditions of OECD devices were fitted with second-order equations (lines).

charges induced on the source in the active layer at 50% DoA). Since the number of lost charges must equate to the number of gained charges on the opposite side of the channel at the applied V_{DS}, the actual values of V^0_D/V^0_S are lower/higher than E^0 (≈0.3 V) according to the aforementioned Equation (1). In the case of the symmetric active layer (i.e., DoA = 50%, black line in Figure 2b), since the capacitance of the active layer on the source (i.e., $E > 0.3$ V) is higher than that on the drain (i.e., $E < 0.3$ V) as shown in Figure 2b, the V^0_S (solid circles) is much smaller than the corresponding V^0_D (open circles), in order to satisfy charge conservation ($Q_D = Q_S$) across the channel. For the asymmetric active layer structures (i.e., DoA > 50%, bluish lines in Figure 2b), the latent capacitance of the drain side increases by the increased amount of active material at higher DoA, while the simultaneous reduction in the active material on the opposite side reduces the latent capacitance on the source side. Therefore, the resultant V^0_D shifted toward the E^0, and V^0_S increased as a result of the fixed V_{DS}. Under a positive V_{DS}, however, both V^0_D and V^0_S shifted negatively as the DoA value increased (see Figure S3a, Supporting Information). Note that the applied potential across the channel (V_{DS}) was fixed at ±0.6 V, to ensure stable device operation (vide infra).

In parallel, our proposed electrochemical diode can be viewed as a gate-less electrochemical transistor, the equivalent circuit model of which consists of two voltage sources; V_{DS} between the drain and source and the virtual gate potential (V'_G) between the electrolyte (vs Ag/AgCl) and source (i.e., $V'_G = -E^0 - V^0_S$, Figure 2c inset). This model allows the potential values to be conventionally described, relative to the highest potential observed in the active layer at negative V_{DS} (i.e., E of the active on the source; V^0_S). Therefore, as the DoA increases, the V^0_S increases gradually in the positive direction (solid circles in Figure 2b) and the corresponding V'_G decreases under negative V_{DS} (bluish circles in Figure S3b, Supporting Information), and the actual potential of the channel (E) is located in the highly conductive and capacitive regime (see Figure 1d). In the case of positive V_{DS}, the highest potential of the active layer is on the drain and, as the DoA increases, V'_G (= $-E^0 - V^0_D$) decreases only slightly in the negative direction (reddish circles in Figure S3b, Supporting Information) where the E still remains in the less conductive regime (see Figure 1d). These combined *I–V* behaviors at negative and positive V_{DS} indicate a conventional diode characteristic; charge conduction is suppressed at positive V_{DS} and permitted at negative V_{DS}. Furthermore, such a diode characteristic becomes more prominent as the coverage of the active layer on the drain surpasses that on the source. Figure 2c shows the resultant V'_G plots under the V_{DS} from –0.6 to +0.6 V while the DoA is varied from 50 (black) to 95% (blue). In particular, as the DoA increases up to ≈100%, the V'_G approaches the curves which consist of $V'_G = -E^0 + V_{DS}$ ($V_{DS} < 0$) and $V'_G = -E^0$ ($V_{DS} > 0$) (dashed lines in Figure 2c), because V^0_S and V^0_D become $-V_{DS}$ and 0 under negative and positive V_{DS} in 100% DoA, respectively. Furthermore, the expected *I–V* characteristic curves of electrochemical diodes are depicted in Figure 2d, by matching the potential values of V_{DS} and V'_G in the OECD (open circles) with those of V_{DS} and V_{GS} of output curves in the OECT (dashed lines; V_{DS} = –0.6 V and V_{GS} = –0.8 to 0 V with 0.05 V interval). These curves (solid lines) which were fitted with second-order equation (i.e., $I_{DS} \propto V_{DS}^2$) confirm that the diode characteristics (i.e., suppressed current under backward bias, enhanced current at forward bias) become more prominent with increased DoA.

For the experimental verification of the asymmetric active layer-induced focused/dispersed doping which is responsible for characteristic diode behavior, we conducted in operando potential mapping via optical imaging, so that actual electrical potential could be measured without artifacts induced by electrical measurements (**Figure 3**a). First, the transmitted light through the OECD device was recorded using an electron-multiplying charge-coupled device (EMCCD) with a bandpass filter

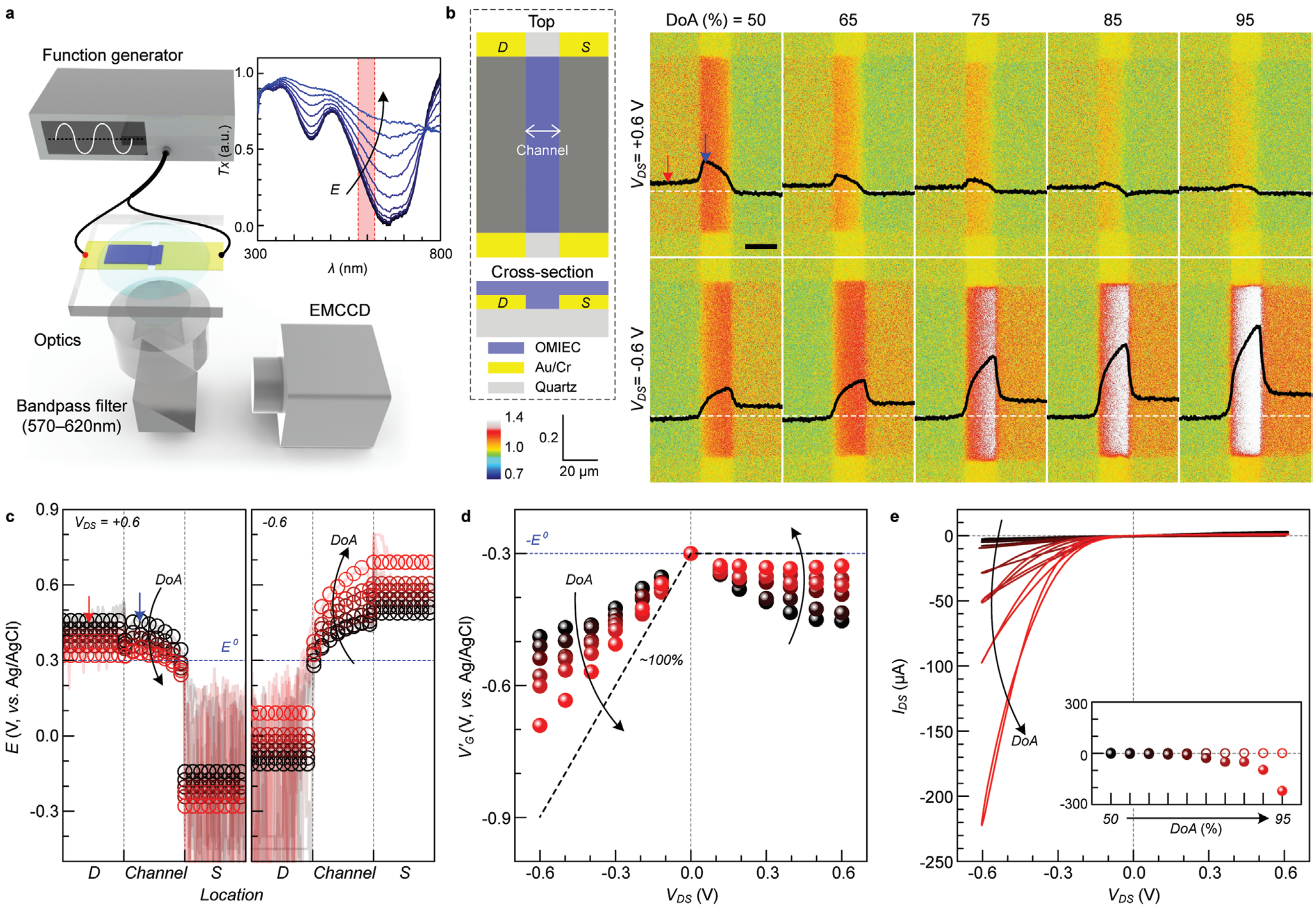

Figure 3. In operando potential mapping and *I–V* characteristics of OECD devices. a) Schematic illustration of in operando optical potential mapping using EMCCD fitted with a bandpass filter (570–620 nm). The inset shows the spectroelectrochemical analysis with *E* gradually scanned from –0.2 (black) to 0.8 V (blue). b) A schematic of device structure (top and cross-sectional views) and series of normalized transmitted light images as a function of DoA (column; 50–95%) and V_{DS} (upper: 0.6 V, lower: –0.6 V) with *x*/*y* dimensions (scale bar: 20 µm) and color-coded relative transmittance. The overlaid line plots represent line-cut profiles of each normalized transmittance distribution across drain/source electrodes. c) Extracted potential profiles across the drain and source using the normalized transmittance profiles and correlation curves at various DoA. d) Extracted V'_G under the V_{DS} from –0.6 to 0.6 V as a function of V_{DS}. e) Experimentally measured *I–V* characteristic curves and on-(solid) and off-(open symbols; inset) current plots as a function of DoA. In (d–f), the data representing increased DoA is shown in black (50%) grading to red (95%).

(570–620 nm). As shown in the spectroelectrochemical analysis of the active layer (PgBT(F)2gTT) on a transparent indium-tin-oxide electrode (*E*; –0.2 to +0.8 V vs Ag/AgCl; Figure 3a inset), the transmittance through the active layer changes according to its electrochemical doping state, which is modulated by varying the applied *E*. When the *E* value is above 0.3 V (i.e., E^0 of PgBT(F)2gTT), the active layer undergoes electrochemical doping, resulting in an increase in the visible region transmittance attributed to the quenching of the polymer S_0–S_1 transition (vice versa). Figure 3b depicts a series of normalized light-transmission images through OECDs of varying DoA from 50% to 95%, where the upper/lower row shows the normalized transmittance at V_{DS} = +0.6/–0.6 V. Color-coded normalized transmittance mapping is achieved by calculating the ratio between the in operando transmittance (at $V_{DS} \neq 0$ V) and the reference transmittance (at $V_{DS} = 0$ V, thereby $E = E^0$). In the case of 50% DoA (i.e., symmetric channel design), the normalized transmittance image at V_{DS} = +0.6 V is the mirror image of that at V_{DS} = –0.6 V; reflective of the fact that when the areal occupancy of the active layer on the drain equates to that on the source, the absolute gradient of charge across the channel at V_{DS} = +0.6 V is the same as that at V_{DS} = –0.6 V. In contrast, as the DoA increases above 50% (i.e., asymmetric channel design), the upper- and lower-row images become dramatically asymmetric. For DoA > 50%, the active layer on the source becomes more doped in the negative V_{DS} regime as indicated by enhanced transparency (i.e., reddish color), thereby, giving rise to a proportional increase in channel conductivity. Note, the intensity variations in the drain and source regions are less prominent than that in the channel region (i.e., gap between the drain and source), due to the light absorption by the underlying metal layer, thus, the attenuated transmission variation (see also the cross-sectional view of the OECD device in Figure 3b inset).

Next, we examined the correlation between the normalized transmittance and the potential of the active layer (*E*, vs Ag/AgCl), so that the areal potential profile could be extracted from Figure 3b (vide infra). While the identical potential (*E*) applied on the drain and source was scanned from –0.2 to +0.8 V (Figure S4, Supporting Information inset), the optical transmittance through the active layer was recorded. Then, we obtain the normalized transmittance values at the channel (i.e., through active only) and the drain/source region (i.e., through active and metal) as the ratio between the nominal transmittance (T) and the transmittance at the reference potential (T_0 at $E = E^0 = 0.3$ V for PgBT(F)2gTT), and plot them as a function of the applied E, as shown in Figure S4 (Supporting Information). The areal potential (E) profiles under positive (left) and negative (right) V_{DS} at various DoA values (black circles; 50%, grading to red circles; 95%, Figure 3c) were extracted from the corresponding line-cuts of normalized transmittance profile (black lines in Figure 3b) using the T/T_0 vs E correlation curve (Figure S4, Supporting Information). The potential estimation at the channel and electrode regions were conducted separately, based on the solid (active)- and open (active/metal)-circle correlation curves. For instance, the normalized transmittance of 1.03/1.13 (red/blue arrow in Figure 3b) at $V_{DS} = +0.6$ V for the device with 50% DoA corresponds to active layer potentials of 0.46/0.46 V (red/blue arrow in Figure 3c). Considering the T/T_0 deviations of 5.0% and 7.5% on active-only and active-metal regions, respectively (Figure S5, Supporting Information), the optically estimated potential values shows a maximum potential deviation of ≈9% in the doped region where the correlation curve between the normalized transmittance and the potential is at its highest slope (Figure S4, Supporting Information). To achieve the high-accuracy potential estimation in the dedoped region, the potential on this region is extracted from the relationship of $V_{DS} = V^0{}_D + V^0{}_S$. At the 50% DoA, the potential distributions at positive and negative V_{DS} appear almost mirror images (black circles) but, when the DoA is incremented up to 95% (reddish circles), the resultant potential distribution at positive V_{DS} is shifted slightly in the negative direction, while that at negative V_{DS} is shifted in the positive direction more prominently. It is worth highlighting that the potential distributions match well with the curves which are simulated using the drift-diffusion model (e.g., gradient potential drop in the overall channel region in the case of conducting regime with high DoA at negative V_{DS}, and rapid potential drop near the drain (at negative V_{DS})/source (at positive V_{DS}) in the case of nonconducting regime with low DoA).[51]

Now that the extracted E values on the drain and source in Figure 3c are equivalent to $V^0{}_D$ and $V^0{}_S$, respectively, and V'_G is plotted in Figure 3d. Indeed, the V'_G vs V_{DS} plots at various DoA metrics closely emulate the overall curves shown in Figure 2c. In particular, as the DoA approaches 100%, the V'_G approaches the theoretical maximum (dashed line). Note that the active layer seems partially less doped/dedoped than as predicted by the numerical analysis (Figure 2), possibly, due to the participation of the channel region in the ionic-charge balance. In the experimental OECD I–V characteristics (Figure 3e and Figure S6a, Supporting Information), as the DoA increases from 50% to 95%, the on-current surges from 2.7 to 220 µA at a negative V_{DS} of –0.6 V (solid circles), while the off-current decreases from 2.9 to 0.7 µA at a positive V_{DS} of +0.6 V (open circles in Figure 3e inset), leading to the enhanced rectification ratio from 0.9 to 314.3 (see also Figure S6b, Supporting Information). Therefore, we can conclude that these diode characteristics match well with those predicted by the numerical analysis.

Furthermore, due to the chemically stable molecular structure and high oxidation potential of PgBT(F)2gTT, the resultant OECD devices showed overall stable operation under prolonged DC (e.g., on-voltage of –0.6 V and off-voltage of 0.6 V for 100 s, Figure S7a,b, Supporting Information) and AC bias stresses (e.g., sinusoidal V_{GS} of 1.2 V_{PP} for 120 cycles, Figure S7c, Supporting Information). However, the slow ionic motion and large electrochemical capacitance in OECD devices make their transient responses slower, such that the ionic current is significantly detected on the pulsed DC signal. To further characterize the transient behavior of OECD devices, the frequency-dependent responses were examined as shown in Figure S8 (Supporting Information). As the driving frequency of V_{DS} is increased up to the cut-off frequency (≈5 Hz), the on-current values showed partially increasing and decreasing trends with the increased negative phase due to the slow response in the ionic-conduction pathway. Furthermore, once the frequency of V_{DS} exceeds the cut-off frequency, the phase becomes positive, and the ionic component becomes dominant in the output current due to the large electrochemical capacitance of OECD devices. Nonetheless, the frequency responses of OECD devices depend on the electronic/ionic capacitive component, so that their performance can be improved further by introducing reduced device dimensions and/or reduced-capacitance active materials which are beyond the scope of this study.

To address whether the proposed mechanism of electrochemical diode operation is generic regardless of the constituent active material, we fabricated/characterized OECD and OECT devices using various types of OMIECs; i) p(g2T-TT); p-type semiconductor, ii) p(NDIMTEG-T); n-type semiconductor, and iii) PEDOT:PSS; p-type conductor. As shown in Figure S9a–c (Supporting Information), all three materials exhibit typical accumulation- or depletion-mode OECT characteristics within the ±1 V_{GS} range as well as E-dependent C^* behaviors (Figures S10 and S11, Supporting Information). In cases of p(g2T-TT) and p(NDIMTEG-T), both transistors show near-zero I_{DS} at $V_{GS} = -E^0$ (dashed line), and the magnitude of I_{DS} grows with increased V_{GS} over $-E^0$. Therefore, when active layers are locally doped/dedoped at the different polarities of V_{DS} in the OECD structure, it is expected that the channels become conductive or nonconductive at opposite-sign bias for the asymmetric channel design. Indeed, both materials exhibited diode-like I–V characteristics (Figure S9d–e, Supporting Information), and the on-/off-current increased/decreased with the increased DoA (Figure S9d,e, Supporting Information inset), similar to PgBT(F)2gTT. The OECD devices based on p(g2T-TT) showed large on-current up to ≈270 µA owing to its outstanding transconductance but high off-current and large hysteresis due to high I_{DS} at $V_{GS} = -E$ and high capacitance at $E = E^0$, respectively (vide infra). In contrast, the devices based on PEDOT:PSS did not show diode behavior because the PEDOT:PSS channel is already in the conductive regime at $E = E^0$ (≈0 V) unlike semiconducting polymers. Note that Chen et al. reported a current rectifying device that consists of a PEDOT:PSS-based active layer pattern, with two locally defined openings as an ionic channel above the active layer, and a gel-type electrolyte.[52] Despite the successful demonstration of current rectification behavior, their rather specific device design could not be generalized to various types of OMIECs, while the in-depth investigation of the underlying operating principle was provided with detailed experimental evidence.

Based on the abovementioned results, we proposed universal design rules for organic-based electrochemical diodes in terms of active layer geometry and material requirements. First, a large DoA can induce highly focused (at forward bias) and dispersed (at backward bias) electrochemical doping at designated active layers, so that the devices exhibit polarity-dependent switching behavior. Note that when the area of active-source contact (A_S) becomes even smaller than the area of channel region, the induced ions interact mainly with the channel region. Accordingly, the potential of the active-source contact ($V^0{}_S$) increases less, thus, the resultant on-current increases less than in the case where the active-source contact is larger than the area of channel region. Second, as A/L (A; cross-sectional area, L; length of the channel) is increased, the on-current is enhanced, as in the case of conventional diodes and transistors, due to short and/or wide active channel. As we demonstrated that the proposed OECD device structure is equivalent to the special case of a gate-less OECT, the overall operation of the OECD could be predicted by the characteristic equations of an OECT. Third, it is highly desired that the corresponding OECT current at $V_{GS} = -E^0$ should be as close to zero as possible to minimize the off-current, thereby necessitating the application of perfect accumulation-mode OECT materials (i.e., semiconducting materials; PgBT(F)2gTT, p(g2T-TT), and p(NDIMTEG-T)). Furthermore, highly asymmetric transconductance, namely, large μC^* at $E > E^0$ and low μC^* at $E = E^0$ leads to maximized on-current and minimal off-current, respectively, in the steady-state operation as demonstrated by the better OECD performance with PgBT(F)2gTT than with p(g2T-TT). Fourth, low capacitance at $E = E^0$ (i.e., $V_{DS} = 0$ V) is necessary for fast transient responses as well as reduced hysteresis, considering the effect of the resistor–capacitor time constant on the ionic current, as exemplified by the PgBT(F)2gTT OECD which exhibits similar forward/backward I–V curves (Figure 3e).[53] Note that the overall capacitance of capacitors in series is governed by the smallest one, such that the capacitance of the active layer on the drain is the dominant factor in the resultant ionic circuit for both forward- and reverse-bias conditions. Lastly, the E^0 of a given active material should be carefully designed to satisfy the aforementioned requirements, and should be sufficiently stable under ambient conditions to prevent uncontrolled oxidation/reduction, thereby, minimizing potential drift during the OECD operation.[49,54]

For a practical demonstration of the aforementioned OECD design rules, particularly, considering that the on-current in a conventional planar OECD (pOECD) device increases with the DoA and A/L, we fabricated a high-performance diode structure with a vertical Corbino channel (vcOECD; **Figure 4**a).[55,56] By defining the channel on a vertical/circular wall of the small via hole ($\phi = 10$ µm) between the drain and source electrodes, A/L and DoA could be increased up to 25% and 99.75%, respectively, compared to the pOECD shown in Figure 1a (see also Figure S12, Supporting Information and Experimental Section). Note that the Corbino device structure is advantageous for the practical demonstration of an OECD device with very large DoA, since the photolithographic definition of the active layer is independent of the mask overlaying error, even with a laboratory-scale mask aligner. Figure 4b depicts J–V characteristic curves of vcOECDs (reddish) in comparison with those of pOECDs (bluish). Due to the geometrical advantage of Corbino structure, the DoA was increased from 95% to 99.75% and, accordingly, the turn-on voltage (–0.166 V) partially approaches the theoretical value (–0.21 V; the detailed extraction method is described in the Supporting Information). Furthermore, the reduced channel length from 20 (pOECD) to 0.25 µm (vcOECD) enabled the on-current density to increase from 1×10^2 to 3×10^4 A cm^{-2}, which is very large in the class of solution-processed organic diodes. It is noteworthy that the OECD is the only high-performance device architecture reported that is capable of rectifying electrical/electrochemical stimuli under aqueous electrolyte having a narrow voltage window of less than 1 V (Figure 4c, and Table S1, Supporting Information).

Finally, we implemented functional analog and digital circuits as a proof-of-concept of broad-impact multifunctional integrated circuitry based on OECDs. As shown in the inset of Figure 4d, a full-wave rectifying circuit was fabricated by patterning four OECDs on the same substrate. As shown in Figure 4e, the sinusoidal analog input voltage signal (black) could be rectified to waves with either positive or negative polarity by using two diodes (V_{node1} and V_{node2}; red) or waves with full polarity by using a four-bridged-diode configuration (V_{out}; blue). Furthermore, we designed representative diode–resistor logic gates, the fundamental building blocks in the modern digital system, which consist of symmetric (50% DoA) and asymmetric (95% DoA) OECDs to define the resistor and diodes, respectively (see Experimental section). Figure 4f,g represents circuit diagrams and truth tables of AND (i), OR (ii), and XOR (iii) logics using symmetric/asymmetric OECDs in a similar manner. As shown in Figure 4h, two digital inputs (A, B) with high (–0.6 V) and low (0 V) signals were applied to each logic circuit, and the resultant voltage outputs from the AND, OR, and XOR logic gates (red, blue, and purple lines) matched well with the theoretical outputs in truth tables. From these results, we believe that the combination of OECDs, OECTs, resistors, and capacitors could broaden the impact of flexible organic analog/digital electronic/ionic systems for various applications such as implantable bioelectronics, neuromorphic circuits, lab-on-a-chips, etc.

3. Conclusions

We have demonstrated high-performance electrochemical diodes based on organic mixed ionic–electronic conductors by introducing asymmetric active layer design on the drain and source electrodes, and verified their working mechanism with in operando potential measurements backed by theoretical modeling. OECD operation could be demonstrated using either p-type or n-type material without complementary material selection or heterojunction formation (e.g., p–n or metal–semiconductor junction), with the only criteria that active materials satisfy the required design rules, for example, accumulation-mode semiconductors with the asymmetric transconductance profile with respect to the corresponding oxidation potential, etc. Furthermore,

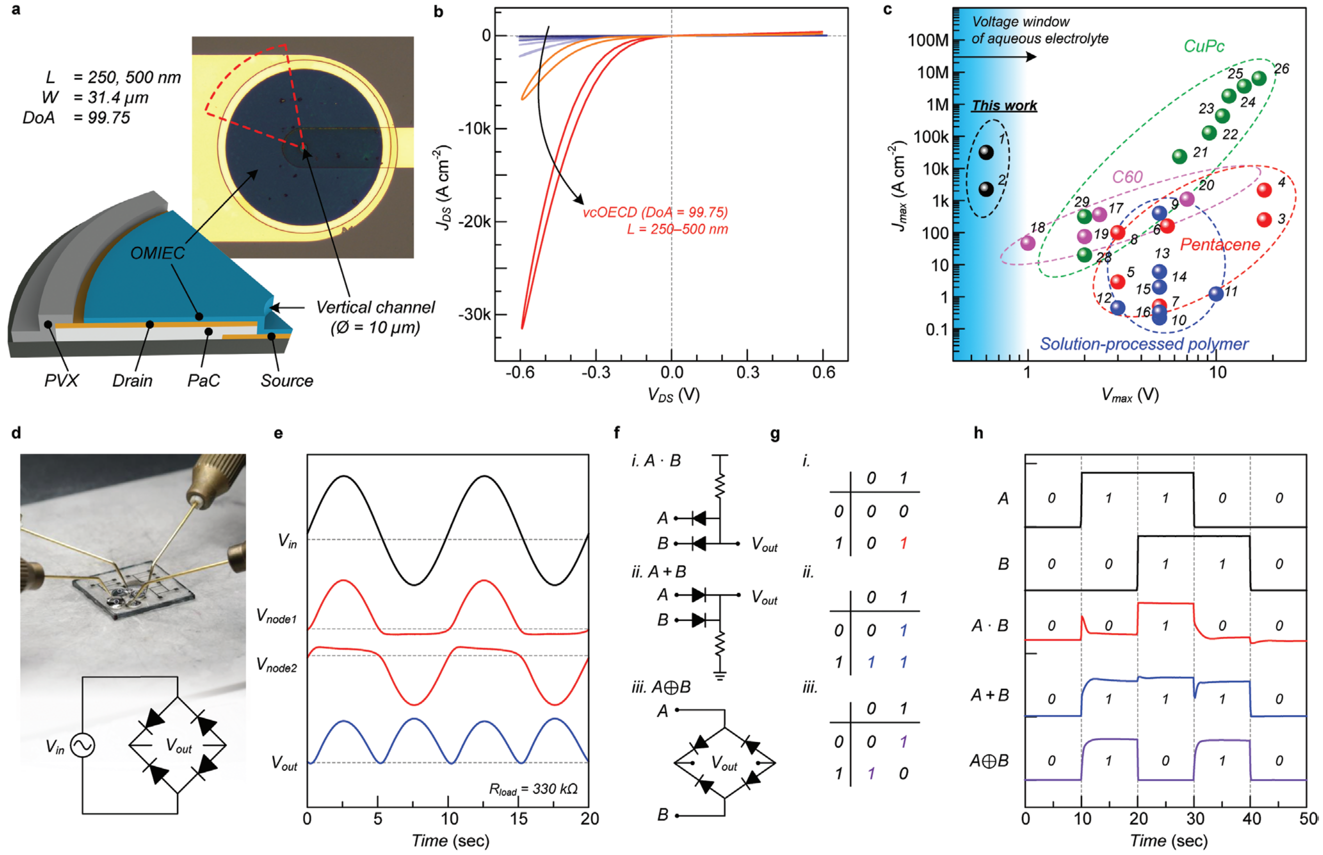

Figure 4. High-performance vcOECD and analog/digital circuit demonstration. a) Photograph and schematic of the vcOECD. The vertically located circular channel along the via hole allows for enhanced DoA (= 99.75%) and reduced channel length ($L = 250$ nm). b) Plots of J–V characteristic curves of vcOECD with a vertical channel length of 0.25 (red) or 0.50 µm (orange) in comparison with those of pOECD (blue). c) A plot of maximum current density (J_{max}) as a function of maximum applied voltage (V_{max}). The detailed information of the labeled number is described in Table S1 (Supporting Information). d) Photograph of OECD-based full-wave rectifying circuit and the corresponding circuit diagram. e) Voltage–time traces of input/output signals through an analog rectification circuit. The sinusoidal signal with dual polarity (black) is passed/blocked through node 1/2 (red) and 4-bridged-diode (blue) so that a clear single-polarity output signal could be acquired. f) Digital logic circuit diagrams and g) corresponding truth tables; (i. AND, ii. OR, and iii. XOR). h) Input (A and B) and output voltage signals with numbers representing 0 (low) and 1 (high) signals.

a route to maximize OECD performance by implementing a vertical Corbino device architecture was presented, leading to a very large current density (>30 kA cm^{-2}) among solution-processable organic heterojunction diode families. Finally, analog voltage rectifying and digital logic processing circuits were demonstrated by fabricating a series of multiple OECDs with proper design rules. We expect that the proposed general design rules of high-performance organic electrochemical diodes will play vital roles in realizing broad-impact soft bioelectronics and power electronics with versatile functions and practical benefits. Particularly, owing to the fabrication compatibility with OMIEC-based passive/active components and environment-sensitive operation in aqueous electrolytes, OECD devices in combination with OECTs can be employed for bioelectric/biochemical sensors and neuromorphic device arrays which can be implanted and operated in physiologically relevant environments.

4. Experimental Section

Materials: Enhancement mode OMIECs (PgBT(F)2gTT, p(g2T-TT), and P(NDIMTEG-T)) were prepared, as previously reported.[8,49] OMIEC powders were dissolved in chloroform (anhydrous, >99%, Sigma-Aldrich) with a concentration of 10, 5, and 10 mg mL^{-1}, respectively. Aqueous PEDOT:PSS solution (PH1000) and sulfuric acid (EP-grade) were purchased from Heraeus and Duksan Chemical, respectively. OMIEC thin films were defined according to the previously reported method.[8,10,49] GXR 601 and SU-8 (2002) for lithography were purchased from AZ Chemicals and Microchem. Fluorocarbon polymer (CYTOP) and solvent (Novec7200) for orthogonal patterning were purchased from AGC and 3M.

Electrochemical/Spectroelectrochemical Characterization of OMIECs: OMIEC thin film was cast on transparent indium-tin-oxide-coated quartz substrates, and they were electrically connected with Cu wires and Ag paste (CANS, Elcoat P-100). Then, metallic parts except for OMIEC layers (≈10 × 10 mm^2) were passivated with dielectric epoxy resin (Alteco, F-301). Thickness and areal size of OMIEC were characterized with the surface profiler (Bruker, DektakXT) and ImageJ software. Electrochemical impedance spectroscopy was conducted by an electrochemical workstation (Metrohm-autolab, PGSTAT 302N) with the three-electrode system (e.g., OMIEC-coated samples on working electrode, Ag/AgCl reference electrode and Pt plate counter electrode) in the aqueous NaCl solution (100 × 10^{-3} M). Sinusoidal signal was scanned from 0.1 to 100 kHz with E_{ac} = 25 mV with a step of E_{dc}. Note that the scanning range for each material is denoted on each impedance–frequency graph (Figure S10, Supporting Information). The spectrum was analyzed by Nova software using the equivalent circuit model consisting of one series resistor (R_s), one parallel resistor (R_p), and one parallel capacitor (C_p). C^* was calculated by normalizing the extracted C_p with the corresponding volume of the OMIECs. Spectroelectrochemistry spectrum was acquired by UV–vis spectroscopy (Implen, NanoPhotometer Pearl), as the potential of OMIECs was controlled from –0.2 to +0.8 V by source-measure unit through Ag/AgCl electrode in 100×10^{-3} м NaCl electrolyte. All the p-type OMIEC materials were characterized in ambient condition, but n-type was in N_2 environment.

Fabrication of OECT, pOECD, and Multiple pOECD-Based Circuits: OECT, pOECD, and pOECD-based circuits were prepared with identical fabrication procedures. First, drain and source metal electrodes (thickness; Au/Cr = 45/5 nm) were defined on the quartz substrates by photolithography and thermal evaporation method. Then, OMIEC thin films were spin-coated as described in previous reports in the literature,[8,10,49] and a CYTOP passivation layer was overcoated on each OMIEC layer. The resultant CYTOP/OMIEC layer was patterned by conventional photolithography and O_2 oxygen plasma etching processes. Subsequently, metal electrodes except an active channel region were passivated with SU-8 polymer (Microchem), and the remaining CYTOP layer on active patterns was striped with fluorocarbon solvent (Novec 7200, 3M). Lastly, reservoirs were defined by attaching 3D-printed cylinder-shaped parts on the channel region with dielectric epoxy resin. Note that reservoir was not defined on OECD-based circuit devices, but electrolyte-droplets were defined on each channel.

Fabrication of Vertical-Corbino OECD Fabrication: Multistacked source electrode (small circular shape; Au/Cr = 45/5 nm)/dielectric layer (parylene-C = 250, 500 nm)/drain electrodes (large circular shape with a small hole; Au/Cr = 45/5 nm) were defined in series by contact aligner, thermal evaporator, and parylene coater (Figure S12i–iii, Supporting Information). Then, vertical holes were defined on the inner dielectric layer with O_2-plasma etching method by using drain patterns as a hard mask (Figure S12iv, Supporting Information), and OMIEC layer was defined on small via holes with an identical method with pOECD (Figure S12v, Supporting Information). Then, metallic parts except for an OMIEC layer and contact pads were passivated with SU-8, and the remaining CYTOP layers were removed by fluorocarbon solvent (Figure S12vi, Supporting Information).

Characterization of OECT, OECD, vcOECD, and Multiple pOECD-Based Analog/Digital Circuits: Transfer and output curves were measured by MATLAB-controlled two source-measure units and Ag/AgCl reference electrode as a gate electrode. Applied bias conditions of V_{DS} and V_{GS} for each OMIEC were described on each figure of transfer and output curves (Figures S1 and S9a–c, Supporting Information). Electrical mobility was acquired by using constant-gate-current method with OECT devices.[7,57] Briefly, gate current (I_{GS}) is applied by source-measure unit (Keithley, 2400) through the Pt counter electrode with a constant current (from 10 to 20 nA) measuring the potential between OMIEC layer and Ag/AgCl gate electrode (V_{GS}), then, drain current (I_{DS}) at small voltage bias (V_{DS}) of 1 mV was monitored by using source-measure unit. Then, transit time (τ_e) on each potential from –0.2 to +0.8 with an interval of 0.05 V was acquired from linearly-fitted curves of the plot of $\mathrm{d}I_{DS}/\mathrm{d}t$ vs I_{GS}, and mobility was extracted according to the equation; $\mu = L^2/\tau_e V_{DS}$, where L is length of the channel (20 µm). OECD I–V characteristic curves were measured by using an arbitrary function generator (Tektronix, AFG3021b), a hand-made unity-gain buffer consisting of an operational amplifier (Texas instrument, LM358), a preamplifier (Stanford research systems, SR570), and a data acquisition system (National Instrument, USB 6356). All the diode characterization was conducted using a sinusoidal voltage signal (–0.6– 0.6) of 0.1 Hz. The current density was obtained by dividing the current by the cross-sectional area of the channel. Electrical characterization of p-type materials was conducted in ambient conditions, but n-type material characterization and device operation were conducted under nitrogen environments to minimize ambient-oxygen-mediated issues.

For circuit characterization, sinusoidal (V_{input} = 1.2 V_{PP}) or pulsed signals (high; –0.6 V, low; 0 V) were generated with an arbitrary function generator and a data acquisition system to demonstrate analog and digital logic circuits, respectively. A load resistor of 330 kΩ was used for the four-bridged-diode configuration (i.e., full-wave rectifier and exclusive-OR gate). Output signals were acquired by using a data acquisition system.

In Operando Optical Potential Mapping: In operando optical potential mapping was conducted by inverted microscopy (IX71, Olympus) with a 20× optical lens, an optical reflective filter (570–620 nm), and an EMCCD (ANDOR, Ixon 3). To measure the transparency as a function of potential (E) of the OMIECs, transmitted light images were acquired under voltage bias from –0.2 to +0.8 V with an Ag/AgCl electrode and a source-measure unit. Relative transmittance (T/T_0) was obtained by dividing the measured transmittance (T) by the transmittance at $E = E^0$ (T_0) during OECD operation. Then, the relative transmittance distribution is converted to potential values with relative transmittance vs E correlation curves. Image processing and analysis were conducted with ImageJ and MATLAB software.

Numerical Analysis: The virtual gate potential (V'_G) was calculated by using the C^* curve (vs E, Figure 2a) and geometrical parameters (e.g., A_D, A_S, and DoA). First, the absolute number of the induced charges ($|Q|$) was calculated from the C^* curve and the corresponding DoA according to Equation (1). Then, shifted drain/source potential (V^0_D and V^0_S) at the applied V_{DS} were acquired from the relationship of $V_{DS} = V^0_D + V^0_S$ and the law of charge conservation (i.e., $Q_D = Q_S$). All the numerical analysis was conducted using MATLAB software.

Supporting Information

Supporting Information is available from the Wiley Online Library or from the author.

Acknowledgements

Y.K., G.K., and B.D. contributed equally to this work. The authors thank the Engineering and Physical Sciences Research Council (EPSRC) (EP/T028513/1), the Royal Society, and the Wolfson Foundation (Royal Society Wolfson Fellowship) for funding. This work was also supported by a National Research Foundation (NRF) grant funded by the Korean government (MSIT) (NRF-2021R1A2C1013015, NRF-2018M3A7B4070988, NRF-2020M3D1A1030660, NRF-2020M1A2A2080748, and NRF-2021R1A4A1022920), the Information Technology Research Center (ITRC) support program (IITP-2021-2020-0-01461) supervised by the Institute for Information & Communications Technology Planning & Evaluation (IITP), the Global Research Laboratory program (NRF-2017K1A1A2013153), and GIST Research Institute (GRI) and GIST Research Project grant by GIST in 2021.

Conflict of Interest

The authors declare no conflict of interest.

Data Availability Statement

Research data are not shared.

Keywords

mixed ionic–electronic conductors, organic diodes, organic electrochemical diodes, organic electrochemical transistors, organic rectifiers

Received: September 15, 2021
Revised: November 12, 2021
Published online: January 10, 2022

[1] A. Giovannitti, C. B. Nielsen, D.-T. Sbircea, S. Inal, M. Donahue, M. R. Niazi, D. A. Hanifi, A. Amassian, G. G. Malliaras, J. Rivnay, I. McCulloch, *Nat. Commun.* **2016**, *7*, 13066.

[2] C. Cendra, A. Giovannitti, A. Savva, V. Venkatraman, I. McCulloch, A. Salleo, S. Inal, J. Rivnay, *Adv. Funct. Mater.* **2019**, *29*, 1807034.

[3] A. Savva, C. Cendra, A. Giugni, B. Torre, J. Surgailis, D. Ohayon, A. Giovannitti, I. McCulloch, E. Di Fabrizio, A. Salleo, J. Rivnay, S. Inal, *Chem. Mater.* **2019**, *31*, 927.

[4] P. Andersson Ersman, D. Nilsson, J. Kawahara, G. Gustafsson, M. Berggren, *Org. Electron.* **2013**, *14*, 1276.

[5] S. Zhang, E. Hubis, G. Tomasello, G. Soliveri, P. Kumar, F. Cicoira, *Chem. Mater.* **2017**, *29*, 3126.

[6] H. Lee, S. Lee, W. Lee, T. Yokota, K. Fukuda, T. Someya, *Adv. Funct. Mater.* **2019**, *29*, 1906982.

[7] S. Inal, G. G. Malliaras, J. Rivnay, *Nat. Commun.* **2017**, *8*, 1767.

[8] A. Giovannitti, D.-T. Sbircea, S. Inal, C. B. Nielsen, E. Bandiello, D. A. Hanifi, M. Sessolo, G. G. Malliaras, I. McCulloch, J. Rivnay, *Proc. Natl. Acad. Sci. USA* **2016**, *113*, 12017.

[9] D. Khodagholy, J. Rivnay, M. Sessolo, M. Gurfinkel, P. Leleux, L. H. Jimison, E. Stavrinidou, T. Herve, S. Sanaur, R. M. Owens, G. G. Malliaras, *Nat. Commun.* **2013**, *4*, 2133.

[10] S.-M. Kim, C.-H. Kim, Y. Kim, N. Kim, W.-J. Lee, E.-H. Lee, D. Kim, S. Park, K. Lee, J. Rivnay, M.-H. Yoon, *Nat. Commun.* **2018**, *9*, 3858.

[11] Y. Kim, H. Noh, B. D. Paulsen, J. Kim, I.-Y. Jo, H. Ahn, J. Rivnay, M.-H. Yoon, *Adv. Mater.* **2021**, *33*, 2007550.

[12] M. Ghittorelli, L. Lingstedt, P. Romele, N. I. Crăciun, Z. M. Kovács-Vajna, P. W. M. Blom, F. Torricelli, *Nat. Commun.* **2018**, *9*, 1441.

[13] M. Sessolo, J. Rivnay, E. Bandiello, G. G. Malliaras, H. J. Bolink, *Adv. Mater.* **2014**, *26*, 4803.

[14] P. Lin, F. Yan, H. L. W. Chan, *ACS Appl. Mater. Interfaces* **2010**, *2*, 1637.

[15] P. Romele, P. Gkoupidenis, D. A. Koutsouras, K. Lieberth, Z. M. Kovács-Vajna, P. W. M. Blom, F. Torricelli, *Nat. Commun.* **2020**, *11*, 3743.

[16] Y. Kim, T. Lim, C.-H. Kim, C. S. Yeo, K. Seo, S.-M. Kim, J. Kim, S. Y. Park, S. Ju, M.-H. Yoon, *NPG Asia Mater.* **2018**, *10*, 1086.

[17] C.-M. Moysidou, C. Pitsalidis, M. Al-Sharabi, A. M. Withers, J. A. Zeitler, R. M. Owens, *Adv. Biol.* **2021**, *5*, 2000306.

[18] C. Cea, G. D. Spyropoulos, P. Jastrzebska-Perfect, J. J. Ferrero, J. N. Gelinas, D. Khodagholy, *Nat. Mater.* **2020**, *19*, 679.

[19] Y. Liang, M. Ernst, F. Brings, D. Kireev, V. Maybeck, A. Offenhäusser, D. Mayer, *Adv. Healthcare Mater.* **2018**, *7*, 1800304.

[20] C. Pitsalidis, M. P. Ferro, D. Iandolo, L. Tzounis, S. Inal, R. M. Owens, *Sci. Adv.* **2018**, *4*, eaat4253.

[21] J. Rivnay, M. Ramuz, P. Leleux, A. Hama, M. Huerta, R. M. Owens, *Appl. Phys. Lett.* **2015**, *106*, 043301.

[22] P. Andersson Ersman, R. Lassnig, J. Strandberg, D. Tu, V. Keshmiri, R. Forchheimer, S. Fabiano, G. Gustafsson, M. Berggren, *Nat. Commun.* **2019**, *10*, 5053.

[23] P. C. Hütter, A. Fian, K. Gatterer, B. Stadlober, *ACS Appl. Mater. Interfaces* **2016**, *8*, 14071.

[24] B. Schmatz, A. W. Lang, J. R. Reynolds, *Adv. Funct. Mater.* **2019**, *29*, 1905266.

[25] D. Majak, J. Fan, M. Gupta, *Sens. Actuators, B* **2019**, *286*, 111.

[26] H. Sun, M. Vagin, S. Wang, X. Crispin, R. Forchheimer, M. Berggren, S. Fabiano, *Adv. Mater.* **2018**, *30*, 1704916.

[27] P. Romele, M. Ghittorelli, Z. M. Kovács-Vajna, F. Torricelli, *Nat. Commun.* **2019**, *10*, 3044.

[28] T. Leydecker, Z. M. Wang, F. Torricelli, E. Orgiu, *Chem. Soc. Rev.* **2020**, *49*, 7627.

[29] S. Steudel, K. Myny, V. Arkhipov, C. Deibel, S. De Vusser, J. Genoe, P. Heremans, *Nat. Mater.* **2005**, *4*, 597.

[30] K. Myny, S. Steudel, P. Vicca, J. Genoe, P. Heremans, *Appl. Phys. Lett.* **2008**, *93*, 093305.

[31] S. G. Higgins, T. Agostinelli, S. Markham, R. Whiteman, H. Sirringhaus, *Adv. Mater.* **2017**, *29*, 1703782.

[32] F. A. Viola, B. Brigante, P. Colpani, G. Dell'Erba, V. Mattoli, D. Natali, M. Caironi, *Adv. Mater.* **2020**, *32*, 2002329.

[33] S. Steudel, S. De Vusser, K. Myny, M. Lenes, J. Genoe, P. Heremans, *J. Appl. Phys.* **2006**, *99*, 114519.

[34] Y. Liu, B. Wolfrum, M. Hüske, A. Offenhäusser, E. Wang, D. Mayer, *Angew. Chem., Int. Ed.* **2013**, *52*, 4029.

[35] Y. Liu, A. Offenhäusser, D. Mayer, *Bioelectrochemistry* **2010**, *77*, 89.

[36] T. Yamamoto, M. Doi, *Nat. Commun.* **2014**, *5*, 4162.

[37] O. J. Cayre, S. T. Chang, O. D. Velev, *J. Am. Chem. Soc.* **2007**, *129*, 10801.

[38] D. Gao, P. S. Lee, *Science* **2020**, *367*, 735.

[39] K. Fu, D. Han, S.-R. Kwon, P. W. Bohn, *ACS Nano* **2018**, *12*, 9177.

[40] W. Guan, R. Fan, M. A. Reed, *Nat. Commun.* **2011**, *2*, 506.

[41] Q. Pu, J. Yun, H. Temkin, S. Liu, *Nano Lett.* **2004**, *4*, 1099.

[42] S.-M. Lim, H. Yoo, M.-A. Oh, S. H. Han, H.-R. Lee, T. D. Chung, Y.-C. Joo, J.-Y. Sun, *Proc. Natl. Acad. Sci. USA* **2019**, *116*, 13807.

[43] M. Li, C. Wang, Z. Liu, Y. Song, D. Li, *Adv. Funct. Mater.* **2021**, *31*, 2104341.

[44] X. Huang, X.-Y. Kong, L. Wen, L. Jiang, *Adv. Funct. Mater.* **2018**, *28*, 1801079.

[45] J. Pu, T. Fujimoto, Y. Ohasi, S. Kimura, C.-H. Chen, L.-J. Li, T. Sakanoue, T. Takenobu, *Adv. Mater.* **2017**, *29*, 1606918.

[46] D. A. Bernards, S. Flores-Torres, H. D. Abruña, G. G. Malliaras, *Science* **2006**, *313*, 1416.

[47] J. Gao, G. Yu, A. J. Heeger, *Appl. Phys. Lett.* **1997**, *71*, 1293.

[48] S. Tang, L. Edman, *Electrochim. Acta* **2011**, *56*, 10473.

[49] B. Ding, G. Kim, Y. Kim, F. D. Eisner, E. Gutiérrez-Fernández, J. Martín, M.-H. Yoon, M. Heeney, *Angew. Chem., Int. Ed.* **2021**, *60*, 19679.

[50] G. Tarabella, C. Santato, S. Y. Yang, S. Iannotta, G. G. Malliaras, F. Cicoira, *Appl. Phys. Lett.* **2010**, *97*, 123304.

[51] K. Tybrandt, I. V. Zozoulenko, M. Berggren, *Sci. Adv.* **2017**, *3*, eaao3659.

[52] M. Chen, D. Nilsson, T. Kugler, M. Berggren, T. Remonen, *Appl. Phys. Lett.* **2002**, *81*, 2011.

[53] J. T. Friedlein, M. J. Donahue, S. E. Shaheen, G. G. Malliaras, R. R. McLeod, *Adv. Mater.* **2016**, *28*, 8398.

[54] A. Giovannitti, R. B. Rashid, Q. Thiburce, B. D. Paulsen, C. Cendra, K. Thorley, D. Moia, J. T. Mefford, D. Hanifi, D. Weiyuan, M. Moser, A. Salleo, J. Nelson, I. McCulloch, J. Rivnay, *Adv. Mater.* **2020**, *32*, 1908047.

[55] M. J. Donahue, A. Williamson, X. Strakosas, J. T. Friedlein, R. R. McLeod, H. Gleskova, G. G. Malliaras, *Adv. Mater.* **2018**, *30*, 1705031.

[56] H. Lee, J.-S. Yoo, C.-D. Kim, I.-J. Chung, J. Kanicki, *IEEE Trans. Electron Devices* **2007**, *54*, 654.

[57] D. A. Bernards, G. G. Malliaras, *Adv. Funct. Mater.* **2007**, *17*, 3538.